

PAPER

# Evidence of defect formation in monolayer MoS<sub>2</sub> at ultralow accelerating voltage electron irradiation

To cite this article: Ajit Kumar Dash *et al* 2023 *2D Mater.* **10** 035002

View the [article online](#) for updates and enhancements.

## You may also like

- [Vibration detection schemes based on absorbance tuning in monolayer molybdenum disulfide mechanical resonators](#)  
Fengnan Chen, Chen Yang, Wenjing Mao et al.
- [Theory of zero-field superconducting diode effect in twisted trilayer graphene](#)  
Harley D Scammell, J I A Li and Mathias S Scheurer
- [Valley and spin accumulation in ballistic and hydrodynamic channels](#)  
M M Glazov

## 2D Materials



### PAPER

# Evidence of defect formation in monolayer MoS<sub>2</sub> at ultralow accelerating voltage electron irradiation

RECEIVED  
9 November 2022

REVISED  
21 March 2023

ACCEPTED FOR PUBLICATION  
27 March 2023

PUBLISHED  
11 April 2023

Ajit Kumar Dash<sup>1</sup>, Hariharan Swaminathan<sup>1</sup>, Ethan Berger<sup>2</sup> , Mainak Mondal<sup>1</sup>, Touko Lehenkari<sup>2</sup>, Pushp Raj Prasad<sup>1</sup>, Kenji Watanabe<sup>3</sup> , Takashi Taniguchi<sup>4</sup>, Hannu-Pekka Komsa<sup>2</sup> and Akshay Singh<sup>1,\*</sup> 

<sup>1</sup> Department of Physics, Indian Institute of Science, Bengaluru, Karnataka 560012, India

<sup>2</sup> Microelectronics Research Unit, University of Oulu, FI-90014 Oulu, Finland

<sup>3</sup> Research Center for Functional Materials, National Institute for Materials Science, Ibaraki 305-0044, Japan

<sup>4</sup> International Center for Materials Nanoarchitectonics, National Institute for Materials Science, Ibaraki 305-0044, Japan

\* Author to whom any correspondence should be addressed.

E-mail: [aksy@iisc.ac.in](mailto:aksy@iisc.ac.in)

**Keywords:** monolayer MoS<sub>2</sub>, scanning electron microscopy, electron beam irradiation, density functional theory (DFT), machine learning force fields (MLFFs), defects, optical spectroscopy

Supplementary material for this article is available [online](#)

### Abstract

Control on spatial location and density of defects in two-dimensional materials can be achieved using electron beam irradiation. Conversely, ultralow accelerating voltages ( $\leq 5$  kV) are used to measure surface morphology, with no expected defect creation. We find clear signatures of defect creation in monolayer MoS<sub>2</sub> at these voltages. Evolution of E' and A<sub>1</sub>' Raman modes with electron dose, and appearance of defect activated peaks indicate defect formation. To simulate Raman spectra of MoS<sub>2</sub> at realistic defect distributions, while retaining density-functional theory accuracy, we combine machine-learning force fields for phonons and eigenmode projection approach for Raman tensors. Simulated spectra agree with experiments, with sulphur vacancies as suggested defects. We decouple defects, doping and carbonaceous contamination using control (hBN covered and encapsulated MoS<sub>2</sub>) samples. We observe cryogenic photoluminescence quenching and defect peaks, and find that carbonaceous contamination does not affect defect creation. These studies have applications in photonics and quantum emitters.

### Abbreviations

2D	two dimensional
TMDs	transition metal dichalcogenides
ML	monolayer
SPEs	single-photon emitters
SEM	scanning electron microscope
FIB	focused ion beam
TEM	transmission electron microscope
e-beam	electron beam
PL	photoluminescence
DFT	density functional theory
MLFFs	machine learning force fields.

### 1. Introduction

Atomically thin TMDs have exciting optoelectronic properties, including direct bandgaps and tightly bound excitonic complexes [1–4]. Defect engineering can further tune optoelectronic properties [5], and enable creation of novel functionalities [6]. In 2D

TMDs, defects can be of zero (vacancies, interstitial atoms, antisites) or one-dimensional (dislocations, line defects) type [7]. Specifically, antisites and point defects in 2D TMDs provide an ideal platform for making spin qubits [8] and SPEs [9–13] respectively. Defects can be unintentionally created during mechanical and chemical exfoliation, or chemical synthesis. Alternatively, defects can be deliberately introduced and spatially controlled by electron (or ion) beam irradiation.

E-beam transfers energy to the sample by elastic and inelastic scattering mechanisms, including sputtering ( $A_{\text{sput}}$ ) and radiolysis (R), and can also lead to carbonaceous contamination (C) (see figure 1(a)). E-beam of energy above knock-on threshold ( $\sim 80$  kV for S atoms) can create chalcogen vacancies by sputtering [7, 14, 15]. FIB can also create defects by atomic sputtering [16–18]. However, additional material removal can occur due to ion beam bombardment. Hence, FIB is not preferable for

controlled defect formation, especially for creating SPEs that require low defect density. Thus, ultra-low e-beam accelerating voltages (1–5 kV) need to be explored for controllably creating defects, while minimizing surrounding lattice damage, resulting in superior SPEs.

Defects are not expected to be created below knock-on voltages, and especially at ultralow electron accelerating voltages. In contrast, there are recent reports of defect formation at low voltages. One proposed mechanism is defect creation due to localization of electronic excitations to emerging defect sites, which reduces displacement threshold energy of sputtering atoms [19]. In another study, 1 kV electron irradiation followed by annealing resulted in nanopores, attributed to carbonaceous contaminants-induced lowering of activation energy of defect creation [20]. Contrary to this observation, Parkin *et al* [15] reported absence of interaction of carbonaceous contaminants with the sample. Further, Yagodkin *et al* [21] recently showed formation of charge-transfer excitons between carbonaceous contaminants and the MoS<sub>2</sub> sample. SPE formation will benefit greatly from understanding of defect formation at ultralow accelerating voltages and effects of carbonaceous contamination [22, 23].

Raman and PL spectroscopy are widely used for determining layer number and material quality. In ML MoS<sub>2</sub>, first-order Raman modes are denoted as E' and A'<sub>1</sub> (instead of E<sub>2g</sub><sup>1</sup> and A<sub>1g</sub> due to altered crystal symmetry in ML) [15, 24, 25]. Typical PL spectrum of ML MoS<sub>2</sub> at room temperature shows A and B excitons at 1.85 eV and 2 eV respectively, with the A peak comprising of neutral excitons (X<sup>0</sup>) and negatively charged trions (X<sup>-</sup>) [4]. With increasing defect concentration in ML MoS<sub>2</sub>, Raman E' peak shifts towards lower wavenumber (*k*), and full width half maximum (FWHM,  $\Gamma$ ) increases [15, 18]. However, A'<sub>1</sub> peak is not significantly affected by mono-sulphur vacancies. Defects can activate ZO and LO peaks, on the left and right shoulder of E' and A'<sub>1</sub> peaks respectively [16, 18, 26]. For high defect densities, LA-band is observed [20]. Upon electron doping, due to strong electron–phonon coupling, A'<sub>1</sub> peak shifts to lower wavenumber with increased  $\Gamma$  [27, 28]. However, E' peak is not significantly affected by electron doping. Defects also result in significant PL quenching of X<sup>0</sup> and B excitons [29], with increase in low-energy defect-bound excitons at cryogenic temperatures.

Quantifying defect types and concentrations based on experimental Raman spectra is challenging, and will greatly benefit from comparison to Raman spectra obtained from DFT. Unfortunately, modelling systems with low concentration of randomly distributed defects require very large supercells, making calculation of phonons and Raman tensors via conventional computational methods impossible. To reduce computational cost of Raman

tensors, Hashemi *et al* [30] recently developed a method (called Raman-tensor weighed  $\Gamma$ -point density of states, denoted RGDOS) based on projection of large supercell phonons onto those of the unit cell, and it has already been applied to Mo<sub>x</sub>W<sub>1-x</sub>S<sub>2</sub> and ZrS<sub>x</sub>Se<sub>1-x</sub> alloys [30, 31], defects in MoS<sub>2</sub> [32], and SnS [33]. There also exist methods to accelerate the calculation of phonons, for example using classical potential [34] or MLFFs [34, 35]. Using projection of vibrations with MLFFs lead to a very efficient scheme to study large supercells containing small density of defects.

We investigate the creation of defects in mechanically exfoliated ML MoS<sub>2</sub> using e-beam irradiation at ultralow accelerating voltages ( $\leq 5$  kV). We employ Raman and PL spectroscopy to characterize and quantify defects, without creating additional defects. Evolution of E' peak with electron dose is attributed to defect formation, whereas A'<sub>1</sub> peak changes are related to interplay of defect formation, doping due to oxygen adsorbates (physisorption and chemisorption) and e-beam. To understand defect types and concentrations, we combine MLFFs and RGDOS methods to simulate Raman spectra of MoS<sub>2</sub> at realistic defect distributions, yet still retaining DFT accuracy. Sulphur vacancies with concentrations up to 2%–3% lead to good agreement with experiments. To decouple effects of oxygen adsorbates, carbonaceous contaminants, and sulphur vacancies, control samples of hBN covered and encapsulated MoS<sub>2</sub> are measured. Similar Raman peak evolution with electron dose for hBN covered and uncovered ML MoS<sub>2</sub> suggests lack of interaction of carbonaceous contaminants with the sample. Quenching in PL intensity with electron dose at both room and cryogenic temperatures, and emergence of defect-bound excitons at cryogenic temperatures confirms defect formation. We observe narrowing of defect-bound exciton peak linewidth with hBN covering and encapsulation, confirming creation of localized defects ideal for quantum applications. Our work demonstrates a simple approach to create localized defects in ML MoS<sub>2</sub> via electron irradiation at ultralow accelerating voltages.

## 2. Results

MoS<sub>2</sub> flakes were mechanically exfoliated from bulk crystal onto SiO<sub>2</sub>/Si substrate using scotch tape method. The inset of figure 1(b) shows optical image of MoS<sub>2</sub> flake on substrate. Layer numbers were determined by measuring flake optical contrast compared to substrate [36]. For pristine ML MoS<sub>2</sub>, E' and A'<sub>1</sub> Raman peaks are 386 cm<sup>-1</sup> and 404 cm<sup>-1</sup> respectively.

To study defect formation at low accelerating voltages, we irradiated different regions of ML MoS<sub>2</sub> with varying electron doses. We fix accelerating voltage to 3 kV, unless mentioned otherwise.

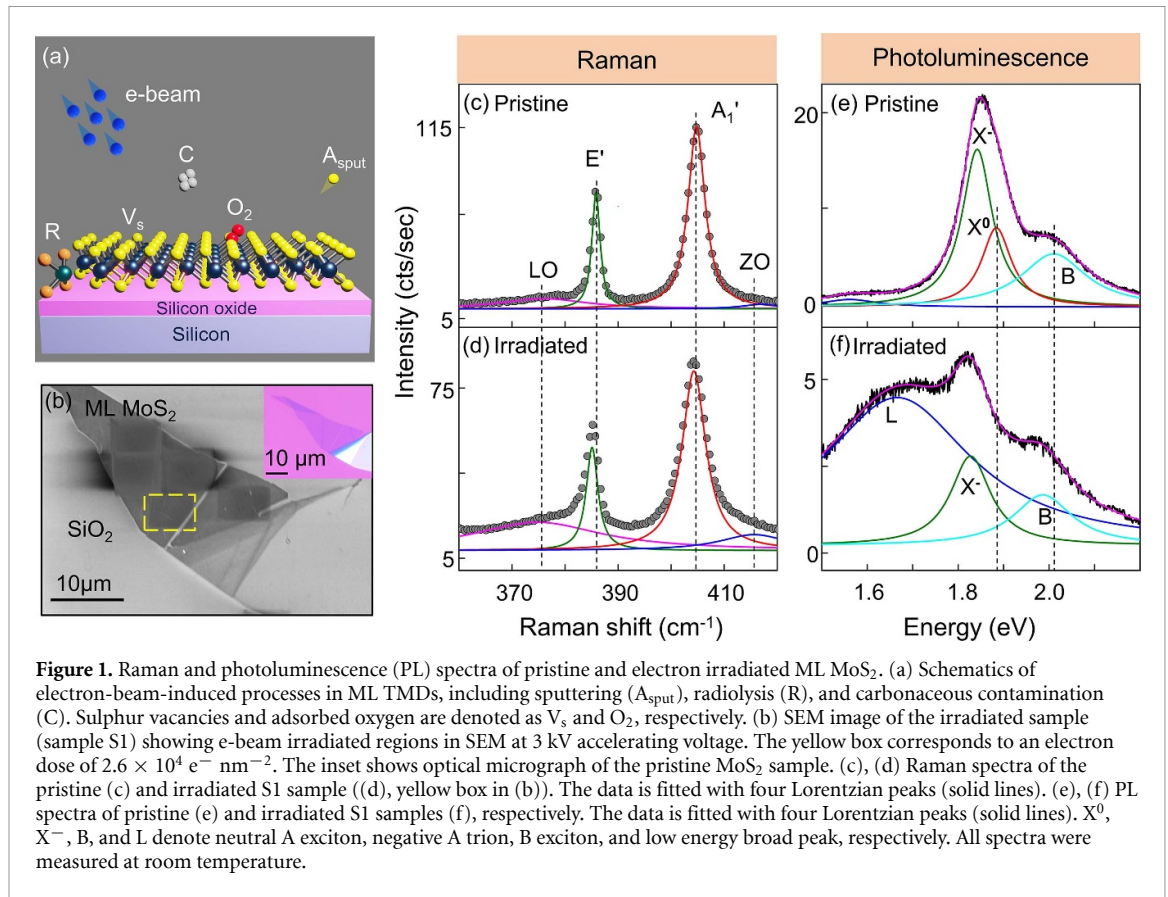


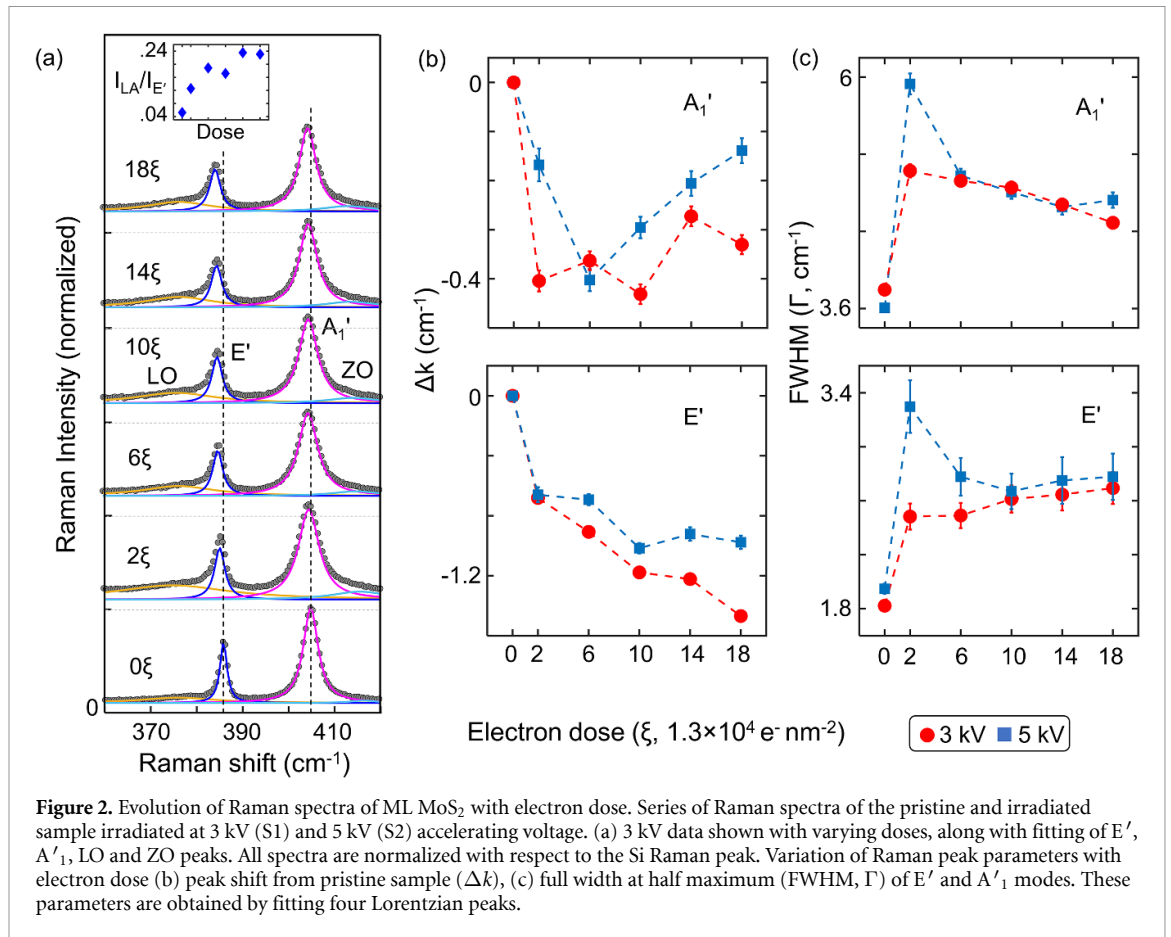
Figure 1(b) shows SEM image of an irradiated sample (S1). The yellow box corresponds to an electron dose of  $2.6 \times 10^4 \text{ e}^- \text{ nm}^{-2}$ . For details of the dose calculation, see supporting information (SI)-III. Carbonaceous contaminants deposited during irradiation result in different contrast for irradiated regions, compared to non-irradiated regions (also confirmed by Raman spectroscopy and atomic force microscopy, for details see SI-VII).

Representative Raman spectra of pristine and electron irradiated samples are presented in figures 1(c) and (d), respectively. Raman spectrum of the irradiated region (yellow box in figure 1(b)) shows redshifts of  $E'$  and  $A'_1$  peaks with respect to the pristine sample even at 3 kV accelerating voltage, well below knock-on voltage for formation of defects in  $\text{MoS}_2$  [14]. Evolution of LO and ZO Raman modes in the irradiated sample (figure 1(d)) is attributed to defects. We note that two and three peak fitting were explored initially, but satisfactory fitting was not achieved. It is important to consider LO and ZO peaks as well (see SI-IV). Defect-induced LA-band ( $\sim 227 \text{ cm}^{-1}$ ) is also observed, but with very low intensity (see SI-VIII), indicating that density of defects created in sample is low.

Figures 1(e) and (f) show PL spectrum of pristine and irradiated ML  $\text{MoS}_2$ , respectively. The overall quenching in PL intensity after irradiation supports the formation of defects [29] and activation of non-radiative decay pathways.  $X^0$  intensity is also

reduced due to conversion to trions via n-type doping by e-beam. An additional broad peak around 1.6 eV was observed in the irradiated sample (figure 1(f)), tentatively labelled as L peak (discussed extensively later). Raman and PL data are also plotted in log-scale to confirm all peaks are accounted for, above the background (see SI-XIX).

To understand defect formation mechanisms, we recorded a series of Raman spectra (figure 2(a)) of ML  $\text{MoS}_2$  irradiated at electron doses ranging from  $0\xi$  to  $18\xi$  ( $\xi = 1.3 \times 10^4 \text{ e}^- \text{ nm}^{-2}$ ,  $0 =$  pristine sample). Raw Raman spectra for all doses are presented in SI-V. The fitting of  $E'$ ,  $A'_1$ , LO and ZO peaks are indicated in figure 2(a). The inset shows integrated LA-band intensity normalized with integrated  $E'$  peak intensity, showing minor contribution of LA-band, which increases with dose (see SI-VIII for details). The evolution of  $k$ ,  $\Gamma$ , wavenumber separation ( $\Delta k$ ), and intensity ratio of  $E'$  and  $A'_1$  peaks with electron dose are tracked. To better understand the evolution of these parameters, we focus on two different dose ranges, (I)  $0-2\xi$ , and (II)  $2\xi$  to  $18\xi$ . In dose range I, we observed redshift of  $k$ , and increased  $\Gamma$  of both  $E'$  and  $A'_1$  peaks (figures 2(b) and (c)). To achieve even lower dose, irradiation was carried out at different magnifications while keeping the same beam current (see SI-XI). The small ( $\leq 0.2 \text{ cm}^{-1}$ ) variations in FWHM of first-order Raman peaks of pristine samples (figure 2(c)) can be attributed to the sample preparation process and local substrate



variations. For example, we observed  $\sim 0.1 \text{ cm}^{-1}$  spatial variations in FWHM across a single sample attributed to variations of local environment. For a particular pristine sample, the indicated FWHM is the mean of FWHMs of different points in the sample. Please also see Raman measurements on other samples in SI-XXI. Further, to study spatial variation in electron irradiated areas, spatial mapping of frequency and FWHM of E' and A<sub>1</sub>'<sub>1</sub> Raman modes were also performed (see SI-XXII for details).

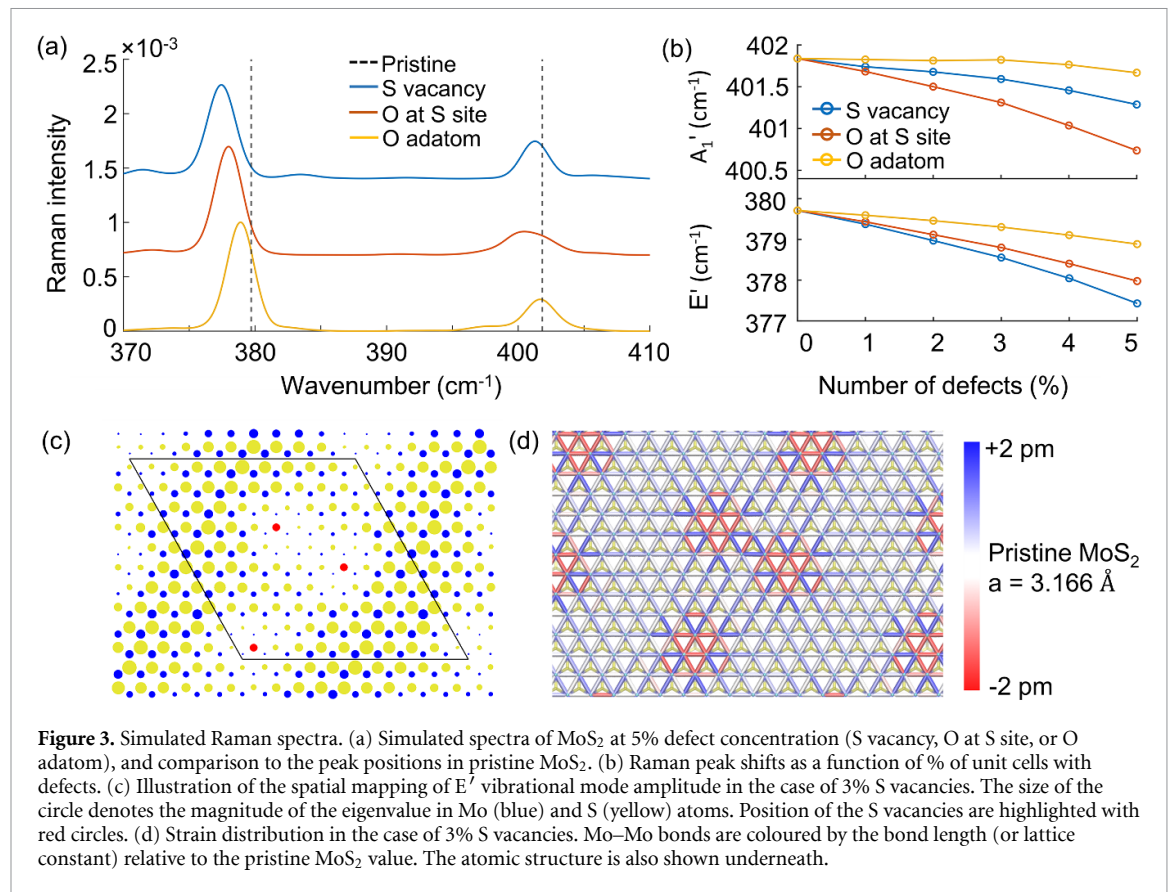
The changes in E' and A<sub>1</sub>'<sub>1</sub> peaks are attributed to defect formation [15, 32] and electron doping [27] respectively. For dose range II, E' peak continues to redshift, attributed to increased sulphur vacancies. In contrast, A<sub>1</sub>'<sub>1</sub> peak blue shifts with decreased  $\Gamma$ , which is attributed to reduced n-type doping due to removal of oxygen atoms from sulphur vacancy sites, and resulting increase of p-type doping due to increased sulphur vacancies. The role of carbonaceous contaminations in Raman spectra evolution is minor, and is discussed later. The increase in peak separation ( $k_{A'_{11}} - k_{E'}$ ) with electron dose (SI-VI) can be attributed to an overall rise in sulphur vacancies [15]. However, if defect formation and doping effects are simultaneously present, separation of E' and A<sub>1</sub>'<sub>1</sub> peaks may not be a good measure of defect formation (also see SI-VI).

To understand accelerating voltage-dependent defect creation, we used two different accelerating

voltages (3 and 5 kV). We did not observe any qualitative differences in 3 kV (sample S1) and 5 kV (sample S2, SI-II) irradiated samples, suggesting similar defect formation mechanisms (also see SI-VI). The intensity ratio ( $I_{E'}/I_{A'_{11}}$ ) of E' and A<sub>1</sub>'<sub>1</sub> modes reduce more for 5 kV irradiation, as compared to 3 kV irradiation (SI-VI).  $\Gamma$  increase is also higher for 5 kV irradiation, compared to 3 kV irradiation. In contrast, wavenumber separation ( $\Delta k$ ) change with electron dose for 3 kV and 5 kV irradiated samples are similar (SI-VI). Overall, irradiation at 5 kV seems to cause slightly more damage than 3 kV irradiation, as also evidenced by room temperature PL data (SI-XX). We note that the comparison of 3 kV vs 5 kV is influenced not just by displacement cross-sections, but by beam width and beam penetration. Suspending samples on a TEM grid may help alleviate this issue, but are beyond the scope of this study.

Recent studies have discussed the reduction of displacement threshold energy of sputtering atoms due to localization of electronic excitations to emerging defect sites [19]. Adsorbed oxygen atoms on sulphur vacancy sites may result in lowering the threshold for damage, by increasing localization of electronic excitations. Further, for ionization and radiolysis processes, the energy transferred to the medium increases as accelerating voltage decreases, scaling as  $1/E$ , then levelling off and eventually decreasing at low acceleration voltages of about 1 kV





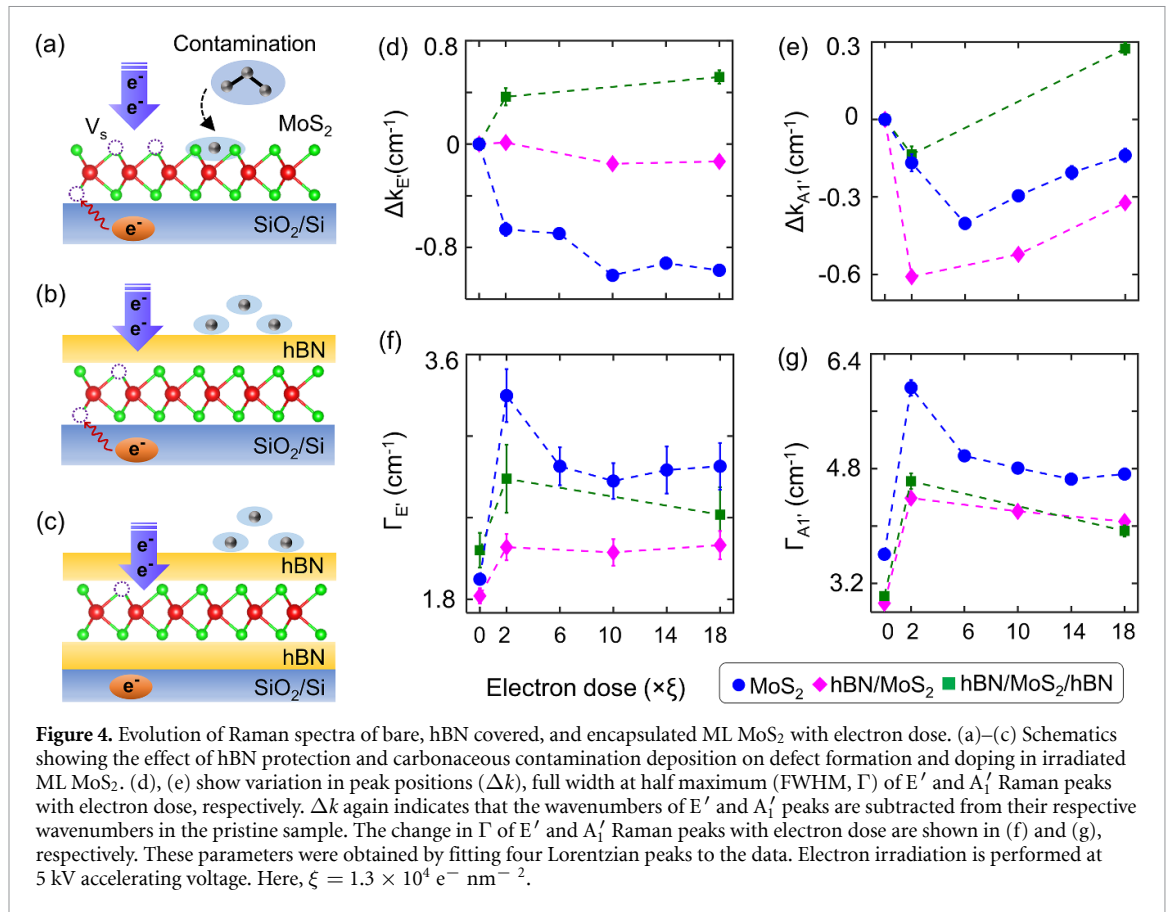
[37]. Since ultralow accelerating voltages are interesting for a growing number of researchers, further theoretical studies are sorely needed for understanding the competing defect formation mechanisms at these voltages (also see SI-XVIII for more discussion on other mechanisms).

To investigate direction and magnitude of the shifts upon introduction of defects, we carried out simulations of Raman spectra based on DFT. Modelling effects of randomly distributed defects on vibrational spectra requires large supercells and to this end, we have adopted two advanced methods. First, MLFFs were trained using small defective systems and with those, the vibrational modes of large supercells could be readily evaluated (for details see SI-I and SI-XIV). Second, Raman tensors of the supercell modes were obtained using RGDOS method, which relies on the projection to unit cell modes and summing up the corresponding Raman tensors. The simulated spectra for three defects, S vacancy, O substitutional in S-site, and O adatom on top of S, at 5% defect concentration are shown in figure 3(a). The simulated spectra for other concentrations, along with added discussion are given in SI-XV and SI-XVI. In addition, the evolution of the peak positions as a function of % of unit cells with defects are shown in figure 3(b).

For S vacancy, E' peak downshifts fairly strongly, which agrees with experimental observations. Quantitatively, 1–1.4 cm<sup>-1</sup> downshift of E' peak would correspond to about 3%–4% vacancy concentration,

which seems reasonable under irradiation conditions considered herein. The E'-mode eigenvector and strain distribution for the case of 3% S vacancies are shown in figures 3(c) and (d). The eigenvector is seen to be localized to regions away from the vacancy. Therein the lattice is tensile-strained, owing to lattice contraction at the vacancy, and this tensile strain translates to a decrease in E' frequency (SI-XVI). The A'1 peak downshifts much less when defects are introduced, which agrees with the much smaller shift with strain. Part of the initial downshift seen in experiments could also arise from vacancies, but the eventual change in direction of the shift cannot, and thus we think this is explained by the doping as discussed above. Extracted peak widths (SI-XVI) indicate stronger broadening for E' peak than A'1 peak, which also qualitatively agrees with experiments.

We also consider a scenario where the sample initially contains O at S-site, which irradiation could effectively turn into S vacancies. Since the downshift of E' peak for O at S-site is only slightly smaller than for S vacancy (0.5 cm<sup>-1</sup> less for 5% defect concentration), such conversion cannot solely explain the experiments, as that would necessitate unrealistically high O concentration of more than 10%. Moreover, that would be accompanied by a large upshift of A'1 peak, inconsistent with experiments. Alternatively, part of the redshift of E' peak could also arise from O adatoms remaining on the surface after leaving the



S-site. The peak shift from adatoms is relatively small but should contribute additively when both adatoms and S vacancies are present.

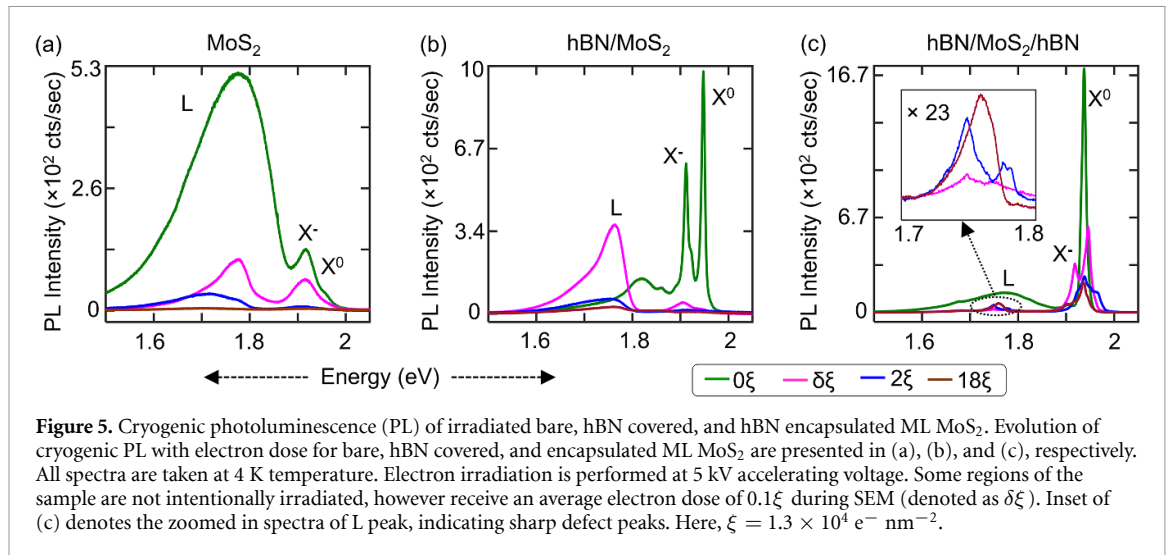
To decouple effects of carbonaceous contaminants and substrate from doping and defect creation, we prepared hBN covered and encapsulated samples (see SI-I and II for methods and optical images). Thickness of hBN ( $\sim 8$  nm) is chosen to allow e-beam interaction with MoS<sub>2</sub>, while restricting carbonaceous contaminants deposition on MoS<sub>2</sub>.

Figure 4 compares E' and A<sub>1</sub>' peak changes with electron dose for bare, hBN covered and hBN encapsulated ML MoS<sub>2</sub>. The possible interactions of these different samples with contaminants and substrate are schematically presented in figures 4(a)–(c).  $k$  and  $\Gamma$  for E' and A<sub>1</sub>' Raman peaks in dose range I and II (figures 4(d)–(g)) have similar trends for bare and covered MoS<sub>2</sub>, suggesting lack of interaction of carbonaceous contaminants with MoS<sub>2</sub>. Hence, decrease in  $\Gamma$  of A<sub>1</sub>' peak in dose range II is not due to carbonaceous contaminant doping effects. Instead, carbonaceous contamination results in increasing Raman background (SI-VII).

Sulphur vacancies in ML MoS<sub>2</sub> are shown to be acceptors [19] and can cause p-type doping [38–40]. In contrast, oxygen adsorption can fill the S-vacancy site, and result in the usually observed n-doping in MoS<sub>2</sub>. Then, removal of oxygen atoms by e-beam can cause reduced n-type doping. As a result, at higher

irradiation time, p-type doping due to sulphur vacancies and removal of oxygen atoms dominates over n-type doping due to e-beam, and causes blue shift and decreased  $\Gamma$  of A<sub>1</sub>'. We note that evolution of E' and A<sub>1</sub>' peak shifts for hBN encapsulated MoS<sub>2</sub> is not consistent across various samples, whereas  $\Gamma$  is consistent (SI-IX). The various doping processes involved in the electron irradiation of MoS<sub>2</sub> and their contribution for dose range I and II are illustrated in SI-XII. Further, Monte Carlo simulations of electron trajectories are performed at 3 kV accelerating voltage using CASINO software [41], providing insights into interaction of e-beam with ML MoS<sub>2</sub> in presence of hBN and carbonaceous contamination (SI-X), and back-scattered electrons (SI-XVII).

PL spectroscopy gives direct insights into the MoS<sub>2</sub> excitonic states, including intra-gap defect-bound excitons. To decouple defect formation and doping effects, we measured cryogenic PL (4 K) of the three irradiated samples i.e. bare, hBN covered, and encapsulated ML MoS<sub>2</sub>. The cryogenic PL of pristine bare ML MoS<sub>2</sub> (figure 5(a), 0 $\xi$ ) shows X<sup>0</sup> and X<sup>-</sup> peaks, and a broad PL peak (L, 1.75 eV) corresponding to adsorbates bound to chalcogen vacancies [42]. A slight exposure of e-beam or mild annealing can remove the adsorbates and open the MoS<sub>2</sub> surface for defect formation. Evolution of PL spectra with electron dose for irradiated bare ML MoS<sub>2</sub> is shown in figure 5(a). The quenching



**Figure 5.** Cryogenic photoluminescence (PL) of irradiated bare, hBN covered, and hBN encapsulated ML MoS<sub>2</sub>. Evolution of cryogenic PL with electron dose for bare, hBN covered, and encapsulated ML MoS<sub>2</sub> are presented in (a), (b), and (c), respectively. All spectra are taken at 4 K temperature. Electron irradiation is performed at 5 kV accelerating voltage. Some regions of the sample are not intentionally irradiated, however receive an average electron dose of  $0.1\xi$  during SEM (denoted as  $\delta\xi$ ). Inset of (c) denotes the zoomed in spectra of L peak, indicating sharp defect peaks. Here,  $\xi = 1.3 \times 10^4 \text{ e}^- \text{ nm}^{-2}$ .

of PL intensity with electron dose is attributed to defect formation and activation of nonradiative decay channels.

The cryogenic PL spectrum of pristine hBN covered MoS<sub>2</sub> (figure 5(b),  $0\xi$ ) shows well distinguished X<sup>0</sup> and X<sup>-</sup> peaks, along with a diminished L peak, indicative of high sample quality. For low electron dose ( $\delta\xi$ ), reduction in X<sup>0</sup> and X<sup>-</sup> peak intensity is observed, along with increase in broad L peak. With further increase in electron dose, high PL quenching is attributed to increase in defect density. The PL spectrum of pristine encapsulated ML MoS<sub>2</sub> (figure 5(c),  $0\xi$ ) shows X<sup>0</sup> peak along with low intensity broad L peak. The absence of X<sup>-</sup> peak is due to blockage of charge transfer from SiO<sub>2</sub>/Si substrate by bottom hBN layer. For low electron dose (figure 5(c),  $\delta\xi$ ), the X<sup>0</sup> PL intensity is quenched along with appearance of X<sup>-</sup> peak, attributed to defect formation and electron doping respectively. With further increase in electron dose, the excitonic PL continues to quench and relative intensity of L peak increases due to increase in sample defect density. However, the extent of damage (compared to bare and hBN covered ML MoS<sub>2</sub>) has reduced due to hBN encapsulation [43]. Further, inset of figure 5(c) shows sharp defect peaks in irradiated encapsulated samples. The hBN layer protects the created defect sites from surrounding environment and substrate, and thus, defect density and linewidth of defect-bound excitons are reduced. These sharp peaks may be promising for SPEs, but detailed studies are beyond the scope of this paper. Power and temperature dependent studies signifies bound nature of the L peak (SI-XIII). L peak shows linear dependence with laser power for bare and hBN covered samples (due to high density of defects), but saturates for hBN encapsulated samples. Also, the intensity of L peak reduces with temperature, signifying the defect origin. Further, appearance of L peak in PL spectra of all irradiated samples (bare,

hBN covered, and encapsulated ML MoS<sub>2</sub>) confirms that L peak corresponds to excitons bound to sulphur vacancies (or other defects) and the interaction of carbonaceous contaminants with sample is negligible.

### 3. Conclusion

We have demonstrated defect formation in ML MoS<sub>2</sub> by e-beam irradiation at ultralow electron accelerating voltages (3–5 kV), and characterized the defects using Raman and PL spectroscopy. The evolution of E' and A<sub>1</sub>' Raman modes and overall quenching in PL intensity indicate defect formation. Defect formation also activates ZO and LO Raman peaks. We have developed a model for simulating Raman spectra in low defect density samples, using a combination of DFT and MLFF calculations, with good agreement with experiments. Further, we decoupled doping effects due to carbonaceous contaminants, defect creation and e-beam using hBN covered and encapsulated MoS<sub>2</sub> control samples. Carbonaceous contaminants do not participate in defect creation or contribute to PL. Interestingly, defect density and corresponding PL linewidth of defect-bound excitons can be reduced via hBN covering and encapsulation. Our work demonstrates a novel approach for creating isolated defects using ultralow electron accelerating voltages in 2D materials ideal for quantum applications. We hope our work will motivate researchers to perform further studies for understanding the defect formation mechanism at ultralow electron accelerating voltages [44].

### Data availability statement

All data that support the findings of this study are included within the article (and any supplementary files).




## Acknowledgments

A S would like to acknowledge funding from Indian Institute of Science start-up and SERB Grant (SRG-2020-000133). AKD would like to acknowledge Prime Minister's Research Fellowship (PMRF). The authors also acknowledge Micro Nano Characterization Facility (MNCF), Centre for Nano Science and Engineering (CeNSE) for use of characterization facilities. The authors also acknowledge Arindam Ghosh Lab (IISc) for use of Raman facility. T L acknowledges financial support from Infotech Oulu Doctoral Program. We gratefully acknowledge CSC-IT Center for Science, Finland, for computational resources. T T acknowledges support from the JSPS KAKENHI (Grant Numbers 19H05790 and 20H00354) and A3 Foresight by JSPS.

## Author contributions

A K D and A S developed the experimental framework. E B, T L and H P K performed the DFT and MLFF modelling of defects. A K D performed the optical experiments and electron beam irradiation, with assistance from H S, M M and P R P. A K D performed the data analysis, with assistance in PL analysis by H S. K W and T T provided the hBN bulk crystals. A K D, H P K and A S discussed and prepared the manuscript, with contributions from all authors.

## ORCID iDs

Ethan Berger  <https://orcid.org/0000-0001-9143-4493>

Kenji Watanabe  <https://orcid.org/0000-0003-3701-8119>

Akshay Singh  <https://orcid.org/0000-0003-1059-065X>

## References

- [1] Splendiani A, Sun L, Zhang Y, Li T, Kim J, Chim C-Y, Galli G and Wang F 2010 Emerging photoluminescence in monolayer MoS<sub>2</sub> *Nano Lett.* **10** 1271–5
- [2] Kośmider K, González J W and Fernández-Rossier J 2013 Large spin splitting in the conduction band of transition metal dichalcogenide monolayers *Phys. Rev. B* **88** 245436
- [3] He K, Kumar N, Zhao L, Wang Z, Mak K F, Zhao H and Shan J 2014 Tightly bound excitons in monolayer WSe<sub>2</sub> *Phys. Rev. Lett.* **113** 026803
- [4] Mak K F, He K, Lee C, Lee G H, Hone J, Heinz T F and Shan J 2013 Tightly bound trions in monolayer MoS<sub>2</sub> *Nat. Mater.* **12** 207–11
- [5] Tongay S et al 2013 Defects activated photoluminescence in two-dimensional semiconductors: interplay between bound, charged and free excitons *Sci. Rep.* **3** 2657
- [6] Wang D, Li X-B, Han D, Tian W Q and Sun H-B 2017 Engineering two-dimensional electronics by semiconductor defects *Nano Today* **16** 30–45
- [7] Dash A K, Mondal M, Verma M, Kumar K S and Singh A 2021 Effect of electron-irradiation on layered quantum materials *Bull. Mater. Sci.* **44** 227
- [8] Tsai J-Y, Pan J, Lin H, Bansil A and Yan Q 2022 Antisite defect qubits in monolayer transition metal dichalcogenides *Nat. Commun.* **13** 492
- [9] He Y-M et al 2015 Single quantum emitters in monolayer semiconductors *Nat. Nanotechnol.* **10** 497–502
- [10] Koperski M, Nogajewski K, Arora A, Cherkez V, Mallet P, Veuillen J-Y, Marcus J, Kossacki P and Potemski M 2015 Single photon emitters in exfoliated WSe<sub>2</sub> structures *Nat. Nanotechnol.* **10** 503–6
- [11] Ye Y, Dou X, Ding K, Chen Y, Jiang D, Yang F and Sun B 2017 Single photon emission from deep-level defects in monolayer WSe<sub>2</sub> *Phys. Rev. B* **95** 245313
- [12] Chakraborty C, Goodfellow K M and Vamivakas A N 2016 Localized emission from defects in MoSe<sub>2</sub> layers *Opt. Mater. Express* **6** 2081–7
- [13] Klein J et al 2019 Site-selectively generated photon emitters in monolayer MoS<sub>2</sub> via local helium ion irradiation *Nat. Commun.* **10** 2755
- [14] Komsa H-P, Kotakoski J, Kurasch S, Lehtinen O, Kaiser U and Krashennnikov A V 2012 Two-dimensional transition metal dichalcogenides under electron irradiation: defect production and doping *Phys. Rev. Lett.* **109** 035503
- [15] Parkin W M, Balan A, Liang L, Das P M, Lamparski M, Naylor C H, Rodriguez-Manzo J A, Johnson A T C, Meunier V and Drndić M 2016 Raman shifts in electron-irradiated monolayer MoS<sub>2</sub> *ACS Nano* **10** 4134–42
- [16] Fujisawa K et al 2021 Quantification and healing of defects in atomically thin molybdenum disulfide: beyond the controlled creation of atomic defects *ACS Nano* **15** 9658–69
- [17] Zhang M et al 2021 Super-resolved optical mapping of reactive sulfur-vacancies in two-dimensional transition Metal Dichalcogenides *ACS Nano* **15** 7168–78
- [18] Mignuzzi S, Pollard A J, Bonini N, Brennan B, Gilmore I S, Pimenta M A, Richards D and Roy D 2015 Effect of disorder on Raman scattering of single-layer MoS<sub>2</sub> *Phys. Rev. B* **91** 195411
- [19] Kretschmer S, Lehnert T, Kaiser U and Krashennnikov A V 2020 Formation of defects in two-dimensional MoS<sub>2</sub> in the transmission electron microscope at electron energies below the knock-on threshold: the role of electronic excitations *Nano Lett.* **20** 2865–70
- [20] Ke J-A, Garaj S and Gradečak S 2019 Nanopores in 2D MoS<sub>2</sub>: defect-mediated formation and density modulation *ACS Appl. Mater. Interfaces* **11** 26228–34
- [21] Yagodkin D et al 2022 Extrinsic localized excitons in patterned 2D semiconductors *Adv. Funct. Mater.* **32** 2203060
- [22] Su C et al 2022 Tuning colour centres at a twisted hexagonal boron nitride interface *Nat. Mater.* **21** 896–902
- [23] Kumar A, Cholsuk C, Zand A, Mishuk M N, Matthes T, Eilenberger F, Suwanna S and Vogl T Localized creation of yellow single photon emitting carbon complexes in hexagonal boron nitride (arXiv:2208.13488)
- [24] Li H, Zhang Q, Yap C C R, Tay B K, Edwin T H T, Olivier A and Baillargeat D 2012 From bulk to monolayer MoS<sub>2</sub>: evolution of Raman scattering *Adv. Funct. Mater.* **22** 1385–90
- [25] Lee C, Yan H, Brus L E, Heinz T F, Hone J and Ryu S 2010 Anomalous lattice vibrations of single- and few-layer MoS<sub>2</sub> *ACS Nano* **4** 2695–700
- [26] Lee J-Y, Kim J H, Jung Y, Shin J C, Lee Y, Kim K, Kim N, van der Zande A M, Son J and Lee G-H 2021 Evolution of defect formation during atomically precise desulfurization of monolayer MoS<sub>2</sub> *Commun. Mater.* **2** 1–10
- [27] Chakraborty B, Bera A, Muthu D V S, Bhowmick S, Waghmare U V and Sood A K 2012 Symmetry-dependent phonon renormalization in monolayer MoS<sub>2</sub> transistor *Phys. Rev. B* **85** 161403
- [28] Rao R, Carozo V, Wang Y, Islam A E, Perea-Lopez N, Fujisawa K, Crespi V H, Terrones M and Maruyama B 2019 Dynamics of cleaning, passivating and doping monolayer MoS<sub>2</sub> by controlled laser irradiation *2D Mater.* **6** 045031
- [29] Kang N, Paudel H P, Leuenberger M N, Tetard L and Khondaker S I 2014 Photoluminescence quenching in

- single-layer MoS<sub>2</sub> via oxygen plasma treatment *J. Phys. Chem. C* **118** 21258–63
- [30] Hashemi A, Krashennikov A V, Puska M and Komsa H-P 2019 Efficient method for calculating Raman spectra of solids with impurities and alloys and its application to two-dimensional transition metal dichalcogenides *Phys. Rev. Mater.* **3** 023806
- [31] Oliver S M, Fox J J, Hashemi A, Singh A, Cavalero R L, Yee S, Snyder D W, Jaramillo R, Komsa H-P and Vora P M 2020 Phonons and excitons in ZrSe<sub>2</sub>-ZrS<sub>2</sub> alloys *J. Mater. Chem. C* **8** 5732–43
- [32] Kou Z, Hashemi A, Puska M J, Krashennikov A V and Komsa H-P 2020 Simulating Raman spectra by combining first-principles and empirical potential approaches with application to defective MoS<sub>2</sub> *Npj Comput. Mater.* **6** 1–7
- [33] Sutter P, Komsa H P, Lu H, Gruverman A and Sutter E 2021 Few-layer tin sulfide (SnS): controlled synthesis, thickness dependent vibrational properties, and ferroelectricity *Nano Today* **37** 101082
- [34] Jinnouchi R, Karsai F and Kresse G 2019 On-the-fly machine learning force field generation: application to melting points *Phys. Rev. B* **100** 014105
- [35] Jinnouchi R, Lahnsteiner J, Karsai F, Kresse G and Bokdam M 2019 Phase transitions of hybrid perovskites simulated by machine-learning force fields trained on the fly with Bayesian inference *Phys. Rev. Lett.* **122** 225701
- [36] Mondal M, Dash A K and Singh A 2022 Optical microscope based universal parameter for identifying layer number in two-dimensional materials *ACS Nano* **16** 14456–62
- [37] Joy D C and Luo S 1989 An empirical stopping power relationship for low-energy electrons *Scanning* **11** 176–80
- [38] Yang J, Kawai H, Wong C P Y and Goh K E J 2019 Electrical doping effect of vacancies on monolayer MoS<sub>2</sub> *J. Phys. Chem. C* **123** 2933–9
- [39] Trainer D J, Nieminen J, Bobba F, Wang B, Xi X, Bansil A and Iavarone M 2022 Visualization of defect induced in-gap states in monolayer MoS<sub>2</sub> *npj 2D Mater. Appl.* **6** 1–7
- [40] Vancsó P, Magda G Z, Petó J, Noh J-Y, Kim Y-S, Hwang C, Biró L P and Tapasztó L 2016 The intrinsic defect structure of exfoliated MoS<sub>2</sub> single layers revealed by scanning tunneling microscopy *Sci. Rep.* **6** 29726
- [41] Hovington P, Drouin D and Gauvin R 1997 CASINO: a new Monte Carlo code in C language for electron beam interaction—part I: description of the program *Scanning* **19** 1–14
- [42] Mitterreiter E *et al* 2021 The role of chalcogen vacancies for atomic defect emission in MoS<sub>2</sub> *Nat. Commun.* **12** 3822
- [43] Singh A, Lee H Y and Gradečák S 2020 Direct optical-structure correlation in atomically thin dichalcogenides and heterostructures *Nano Res.* **13** 1363–8
- [44] Susi T, Meyer J C and Kotakoski J 2019 Quantifying transmission electron microscopy irradiation effects using two-dimensional materials *Nat. Rev. Phys.* **1** 397–405